
RICE UNIVERSITY

**Implementation of Hot Electrons in Hybrid
Antenna-Graphene Structures**

by

Yumin Wang

A THESIS SUBMITTED
IN PARTIAL FULFILLMENT OF THE
REQUIREMENTS FOR THE DEGREE
MASTER OF SCIENCE

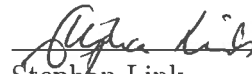
APPROVED, THESIS COMMITTEE:



Peter Nordlander, Chair
Professor of Physics and Astronomy;
Professor of Electrical and Computer
Engineering



Naomi Halas
Stanley C. Moore Professor of Electrical
and Computer Engineering; Professor of
Chemistry; Professor of Physics and
Astronomy



Stephan Link
Assistant Professor of Chemistry;
Assistant Professor of Electrical and
Computer Engineering

Houston, Texas

April, 2013

ABSTRACT

Implementation of Hot Electrons in Hybrid Antenna-Graphene Structures

by

Yumin Wang

Graphene, a one-atom-thick sheet of hexagonally packed carbon atoms, is a novel material with high electron mobility due to its unique linear and gapless electronic band structure. Its broadband absorption and unusual doping properties, along with superb mechanical flexibility make graphene of promising application in optoelectronic devices such as solar cell, ultrafast photodetectors, and terahertz modulators. However, the current performance of graphene-based devices is quite unacceptable owing to serious limitations by its inherently small absorption cross section and low quantum efficiency. Fortunately, nanoscale optical antennas, consisting of closely spaced, coupled metallic nanoparticles, have fascinating optical response since the collective oscillation of electrons in them, namely surface plasmons, can concentrate light into a subwavelength regime close to the antennas and enhance the corresponding field considerably. Given that optical antenna have been applied in various areas such as subwavelength optics, surface enhanced spectroscopies, and sensing, they are also able to assist graphene to harvest visible and near-infrared light with high efficiency. Moreover, the efficient production of hot electrons due to the decay of the surface plasmons can be further implemented to modulate the properties of graphene.

Here we choose plasmonic oligomers to serve as optical antenna since they possess tunable Fano resonances, consisting of a transparency window where scattering

is strongly suppressed but absorption is greatly enhanced. By placing them in direct contact with graphene sheet, we find the internal quantum efficiency of hybrid antenna-graphene devices achieves up to 20%. Meanwhile, doping effect due to hot electron is also observed in this device, which can be used to optically tune the electronic properties of graphene.

Acknowledgments

I would like to thank those people who have always been helping, encouraging and supporting me during past two and a half years. First of all, I want to express my deep gratitude to my advisor, Prof. Peter Nordlander. He taught me how to perform a research systematically, including finding a suitable topic, solving the problem step by step and expressing the entire work clearly. Under his careful guidance, I overcame lots of difficulties and for each time Peter not only provided constructive suggestions and but also brought me confidence. Besides, his many great personalities, such as patience, smartness, strictness, kindness and humor, influenced me and benefited me a lot. Also, I am sincerely grateful to my thesis committee: Prof. Naomi Halas and Prof. Stephan Link for making their valuable time to attend my thesis defense and giving helpful thoughts on my research. Many thanks are due to my former and current groupmates: Dr. Chizuku Dutttta, Dr. Manvir Kushwaha, Dr. Jorge Zuloaga, Dr. Heidar Sobhani, Dr. Ke Zhao, Dr. Nicolas Large, Dr. Kui Bao, Dr. Yang Li, Mr. Yurong Zhen, Mr. Vikram Kulkarni, Mr. Yang Cao, Ms. Lifei Liu. Their valuable discussions are very important for the fulfillment of my projects and thesis. Many thanks are also given to my collaborators, Prof. Pulickel Ajayan, Dr. Zheyu Fang, Dr. Na Liu, Dr. Alexander Urban, Dr. Zheng Liu, Mr. Mark Knight, Ms. Fangfang Wen, Mr. Ali Sobhani. It is a good opportunity to communicate with them and learn lots of experiment details. I also want to thank the Laboratory of Nanophotonics (LANP) and Rice Quantum Institute for providing me such great chances to broaden my knowledge. Furthermore, my deepest gratitude should be given to my lovely family and sincere friends who love me and support me throughout my life. At last, I would like to thank all the funding agencies.

Contents

Abstract	ii
Acknowledgments	iv
List of Illustrations	vii
1 Introduction	1
2 Light Harvesting Assisted by Hot Electrons	4
2.1 Graphene	4
2.2 Surface Plasmons	5
2.3 Graphene-antenna Hybrid Structures	6
2.4 Photocurrent Generation	9
2.5 Plasmonic Enhancement	12
2.6 Quantum Efficiency	15
2.7 Summaries	20
3 Optical Induced Doping with Hot Electrons	21
3.1 Doping and Dirac Point Shift	21
3.2 Observation of Dirac Point Shifting with Absorption	24
3.3 Efficiency of Hot Electron Doping	26
3.4 Saturation of Hot Electron Doping	28
3.5 Optically Induced Electronics	30
3.6 Summaries	31
4 Conclusion	32

Bibliography

Illustrations

2.1	Electronic energy diagram of graphene near Dirac point	5
2.2	Schematic illustration of graphene-antenna hybrid device	7
2.3	Optical microscopy image and scanning electron microscope (SEM) image of graphene-antenna hybrid device	7
2.4	Raman spectra of graphene with plasmonic structures	8
2.5	Electrical transport characteristic of graphene at a drain bias of 1 mV	9
2.6	Local photocurrent measurements for different patterns at 785nm excitation laser	10
2.7	Measured photocurrent for different gate biases	10
2.8	Schematic of the surface potential	11
2.9	Fano resonance in clusters	14
2.10	Selective resonance detection for different sizes of heptamers	15
2.11	Configuration of FDTD simulation	16
2.12	Integral of local field intensity for graphene with and without plasmonic heptamers	17
2.13	Measured photocurrent and its different contributions	18
2.14	Internal quantum efficiency	20
3.1	Electrical transport characteristic $I - V_g$ curve	22
3.2	Schematic of electrostatic doping and hot-electron doping in graphene	22
3.3	Characteristics of Fano resonance in a plasmonic nonamer	24
3.4	Dirac point shift with respect to wavelength of incident laser	25

3.5	Dirac point shift with respect to antenna size	26
3.6	Optical induced carrier density change with respect to Fermi energy for several wavelengths	27
3.7	Dirac point shift varies with incident laser power	28
3.8	Schematics of recombination and scattering processes	29
3.9	Optical induced diode and transistor	30

Chapter 1

Introduction

Plasmonics is a flourishing field of research on the exotic optical properties of metallic structures at the nanoscale [1]. Induced by electromagnetic wave, free electrons at the metal surface perform collective oscillations, quantized as surface plasmons, which in turn can confine the electromagnetic wave in the vicinity of the metals and enhance its field greatly [2]. Therefore, on the one hand, surface plasmon has the ability to manipulate light within a region much smaller than its wavelength which is forbidden conventionally due to the diffraction limit [3, 4]. On the other hand, its highly intensive local field, also known as "hot spot", can assist many optical, physical and chemical processes so as to improve the signals of related devices and techniques significantly, for instance, surface enhanced Raman scattering, light emitting diode, surface enhanced chemical spectroscopy and so on [5–7]. Recently, individual metallic nanoparticles and assemblies thereof have drawn lots of interests because of their unique optical properties arising from localized surface plasmon resonance (LSPR). At resonant frequency, the scattering and absorption cross sections of metallic nanoparticles are enlarged so drastically that they are capable of efficiently harvesting light. Many applications based on that have been demonstrated to improve the efficiency of photovoltaic devices [8, 9] or potentially cure cancer utilizing thermal effects [10, 11]. Moreover, high dependence of resonant frequency on geometries, materials, background dielectrics, mutual interactions and so on, not only enables metallic nanostructures to be actively designed for specific LSPR frequencies [12, 13],

but also make them useful for passive sensing [14, 15]. Due to the rapid development of nanofabrication techniques, numerous complex metallic structures have been reported [16] being precisely designed in order to exhibit fascinating phenomena, such as Fano resonance [13], negative refraction [17], chirality [18] and other unique properties [19, 20].

The life of surface plasmons is relatively short. It can be ended by either reemitting photon into the far-field or generating electron-hole pair. In the latter case, surface plasmons transfer energy nonradiatively to the electrons, therefore, these electrons stay far above the Fermi surface of the metal and are more kinetic than the others [21]. In other words, they are "hot" electrons. Apparently, they have high possibility to go across the interface of the metal and eventually be captured by the other materials next to it. So far, hot electrons or generally speaking hot carriers have been exploited for many applications in terms of photodetection [22], chemical catalysis [23] and bolometers [24]. Since electrons are key elements in circuitry, the nonradiative decay process can be utilized as a natural bridge to connect optical system and electrical system. To this end, the metallic nanostructures act as a true "nanoantenna".

To capture the hot electrons, silicon is usually used although it is not an ideal material because of its low mobility and small mean free path [22]. Nevertheless, a recent new semiconducting material, graphene, is believed to partially overcome this difficulty owing to its high mobility and gapless energy band. The simple configuration of graphene, a one-atom-thick layer of hexagonally packed carbon atoms, grants it peculiar electronic transport characteristics and superb mechanical flexibility, which make it a promising candidate for electronic devices [25, 26]. However, its high transparency, with only 2.3% absorptance in the visible range, makes it no difference from other ordinary materials. Such inherently low absorption cross section

along with poor quantum efficiency seriously limits its performance of implementation in the optical or optoelectronic devices [27]. In order to be efficiently functional in the visible and near-infrared (NI), graphene has to either be modified through geometrical tailoring and electronic doping [28, 29], or be integrated into other optical active materials, such as plasmonic nanoantenna [30, 31].

Here we put plasmonic oligomers and graphene together to investigate how the hot electrons generated influence the properties of hybrid antenna-graphene device. Since plasmonic oligomers are able to provide tunable Fano resonances, arising from the interference of superradiant and subradiant modes [13], they can greatly enhance the nonradiative process. Therefore, a large number of hot electron produced in the plasmonic oligomer is expected to be injected into the graphene. In Chapter 2, we will reveal the effect of hot electrons on the photocurrent production of the device [32]. Detailed simulations enable us to see the quantum efficiency due to hot electron as well as its comparison with direct excitation. In Chapter 3, we focus on how hot electrons dynamically dope the graphene [33]. We will show the relationship between the doping efficiency and the parameters of the plasmonics nanoantenna. Moreover, we will give an estimation on a rough time scale of this doping process. Finally, a brief conclusion will be given.

Chapter 2

Light Harvesting Assisted by Hot Electrons

2.1 Graphene

Graphene is a one-atom-thick material consisting of sp^2 -hybridized carbon atoms arranged in a honeycomb lattice. Since the structure can be regarded as a triangular lattice with a basis of two atoms per unit cell, its first Brillouin Zone forms a hexagon, whose corners are so-called Dirac points. Around the Dirac points, electronic band structure has an approximate form as follows [25],

$$E_{\pm}(\mathbf{q}) \approx \pm v_F |\mathbf{q}| + O[(q/K)^2] \quad (2.1)$$

where \mathbf{q} is the momentum relative to the Dirac points and v_F is the Fermi velocity, K is the magnitude of reciprocal vector. Unlike the usual case, that energy has a quadratic form of momentum: $E(\mathbf{q}) = q^2/(2m_e)$, where m_e is electron mass, the relationship between energy and momentum is linear in the graphene. Therefore, both conduction band and valence band have a cone shape and they touch with each other at the Dirac point, as illustrated in Figure 2.1. The electrons within this regime behave like massless Dirac particles. Because of this, graphene has high mobility which usually achieves 10,000 or even higher. Moreover, parallel and antiparallel directions of pseudospin with respect to directions of the motion of electrons and holes lead to a universal constant optical conductivity $\sigma = \pi e^2/(2h)$, where h is Planck's constant and e is electron charge [34]. Accordingly, the optical absorption is almost a constant, depending on the fine-structure constant only, that is, $\pi\alpha \approx 2.3\%$ [27]. This

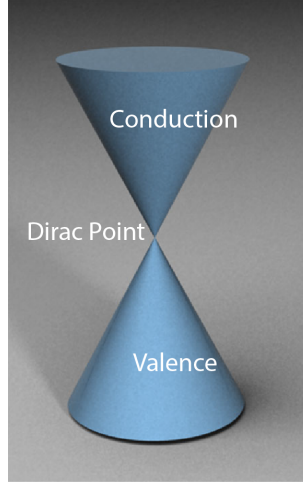


Figure 2.1 : Electronic energy diagram of graphene near Dirac point

is quite remarkable for a single layer material. More interestingly, the absorption can be tuned effectively with suitable doping by either introducing ions or applying gate voltages [35, 36].

2.2 Surface Plasmons

Plasmons are quasi-particles existing in metals and semiconductors, which represent the collective oscillations of electron density. For a bulk metal, the free electron gas can oscillate coherently at a certain frequency, noted as bulk plasmons, $\omega_B = \sqrt{ne^2/\epsilon_0 m_e}$, where n is the density of electrons and ϵ_0 is the permittivity of vacuum [37]. Because of this, metals have strong response to the external optical field which can be expressed in terms of Drude formula:

$$\epsilon(\omega) = \epsilon_\infty - \frac{\omega_B^2}{\omega(\omega + i\gamma)} \quad (2.2)$$

where ϵ_∞ characterizes the background permittivity. This density oscillation can also exist at the interface of metal and dielectrics, which is so-called surface plasmon

(SP). The frequency of SP has strongly geometrical dependence of metal surface, for instance, $\omega_B/\sqrt{2}$ for an infinite planar surface and $\omega_B\sqrt{l/(2l+1)}$ (l is an integer) for a sphere [2, 38]. According to spatial properties, SP can be distinguished into two types. One is surface plasmon polariton (SPP) which propagates along the extended surface such as film or nanowire [3]. The other is localized surface plasmon resonance (LSPR) whose oscillation is localized within nanoparticles [12]. Both plasmons are capable of confining optical field into a region whose dimension is much smaller than the wavelength and meanwhile enhancing its magnitude about 10 to 100 times. The lifetime of plasmon, usually within femosecond, is quite short. Basically, it has two dominant decay processes. One is radiative decay, where the plasmons reemit photons into far-field giving rise to the scattering of the system. The other is non-radiative decay, which corresponds to the absorption or heat generation of the system. During this process, electron-hole pairs are created after plasmons decay and these electrons possess more energy than the rest, so they are regarded as hot electrons.

2.3 Graphene-antenna Hybrid Structures

Our graphene-antenna hybrid device consists of plasmonic clusters sandwiched between two single layers of graphene, shown in Figure 2.2. The fabrication process contains several steps: first, transferring a graphene monolayer onto a SiO₂/Si substrate; then, depositing the source-drain electrodes on the graphene; later, fabricating cluster arrays using e-beam lithography; at last, transferring a second graphene monolayer onto the structures. Figure 2.3 demonstrates the real structures in optical microscopy image and scanning electron microscope (SEM) image. Three different pattern, dimer, heptamer and nonamer, are fabricated for comparison. Raman spectroscopy has been performed for the confirmation of graphene layer by detecting

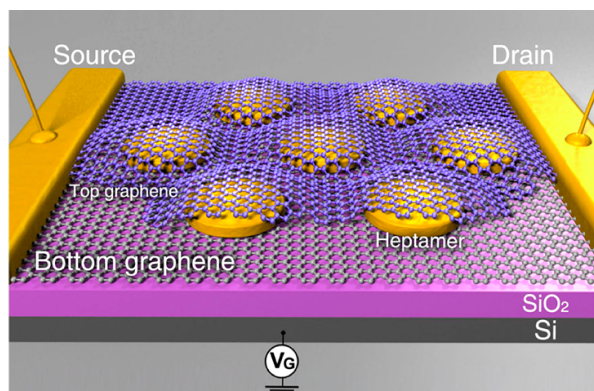


Figure 2.2 : Schematic illustration of graphene-antenna hybrid device

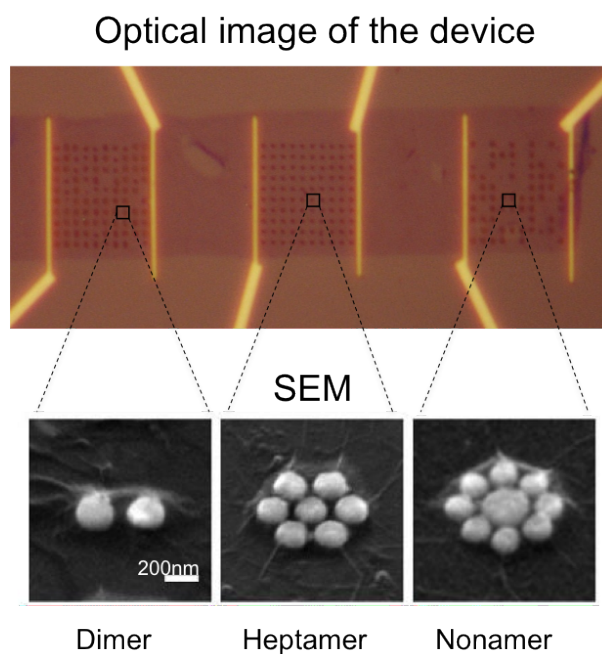


Figure 2.3 : Optical microscopy image and scanning electron microscope (SEM) image of graphene-antenna hybrid device

its characteristic modes (D, G, 2D) with different incident lasers (514nm, 633nm, 785nm), as shown in Figure 2.4 (a), (c) and (e). Raman mappings at G mode in Figure 2.4 (b), (d) and (f) have already revealed that plasmonic structures are able

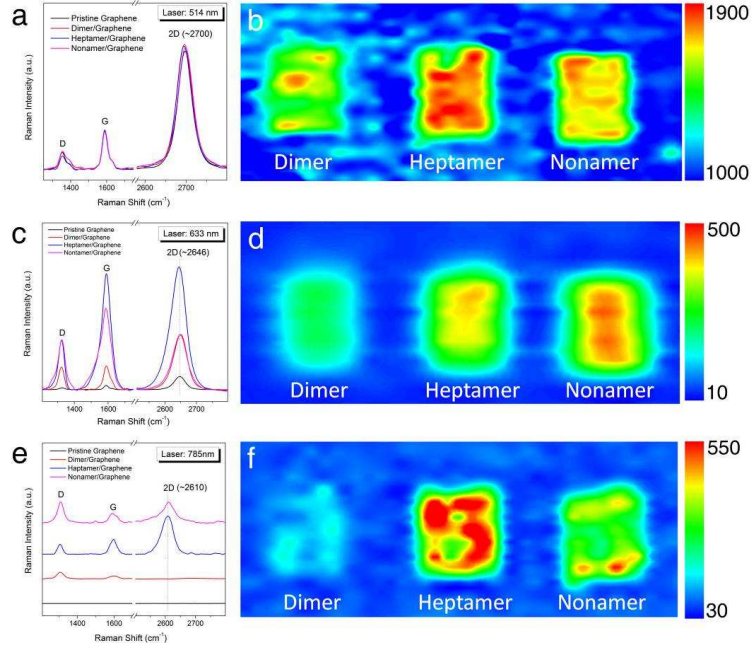


Figure 2.4 : Raman spectra of graphene with plasmonic structures

to selectively enhance the Raman signal from graphene. The quality of graphene is assessed by characterizing its electrical transport properties (Figure 2.5) through four-probe measurement at a vacuum of $\sim 10^{-5}$ Torr. The observed dependence of resistance on gate voltage infers that the Dirac point is obtained at $V_G \sim 30$ V. Based on the linear $I - V$ curve, the device mobility is estimated to range from 350 to 1300 $\text{cm}^2\text{V}^{-1}\text{s}^{-1}$ with formula [39]:

$$\mu = \frac{dI_{DS}}{dV_G} \frac{L}{WC_i V_{DS}} \quad (2.3)$$

where the channel length $L \sim 50\mu\text{m}$, the channel width $W \sim 10\mu\text{m}$ and the real capacitance per unit area between the channel and the backgate $C_i \sim 1.2 \times 10^{-8} \text{F}/\text{cm}^2$.

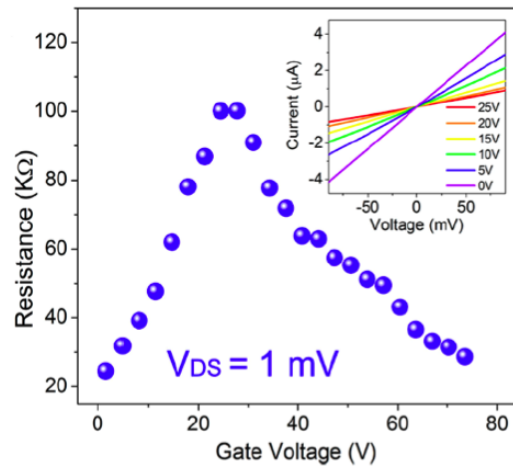


Figure 2.5 : Electrical transport characteristic of graphene at a drain bias of 1 mV

2.4 Photocurrent Generation

To characterize the performance of light harvesting of this device, a series of local photocurrent measurements have been carried out to offer a spatial mapping of photocurrent production. The excitation laser is focused into a spot of $1 \mu\text{m}$ in order to only cover a single optical antenna. By scanning the laser from drain to source, the distribution of photocurrent production with respect to position is registered as shown in Figure 2.6. It has an obvious antisymmetric lineshape and indicates the performance of photocurrent generation is more efficient at certain distance away from the electrodes while it is less efficient at the midpoint of the whole device. Besides, the lineshape can be further tuned by applying a gate voltage. As we can see from Figure 2.7, a negative gate voltage improves the photocurrent generation while a positive one reduces it or even changes its sign, which means the photocurrent flowing in an opposite direction. To better understand the mechanism of photocurrent generation as well as its dependence on gate voltage, we refer to the band structure of our

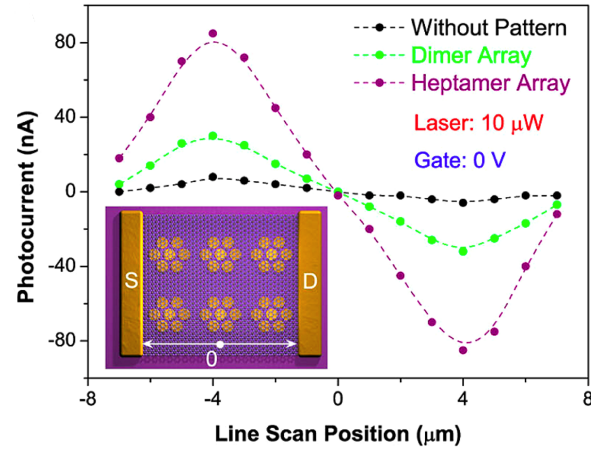


Figure 2.6 : Local photocurrent measurements for different patterns at 785nm excitation laser

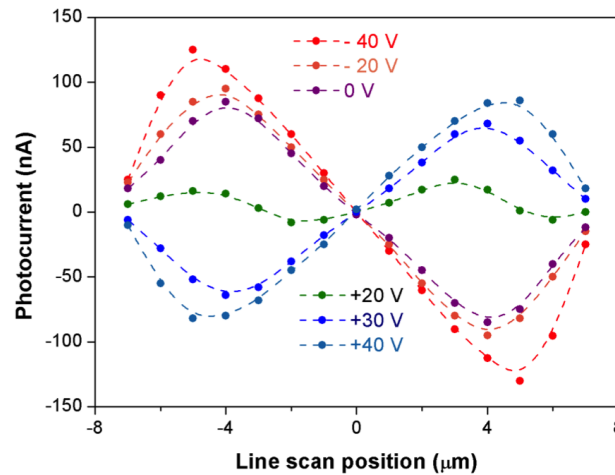


Figure 2.7 : Measured photocurrent for different gate biases

device, as depicted in Figure 2.8. Here, only half of the band is plotted because of the symmetry. The solid line indicates the Dirac point of graphene while the dash line represents its Fermi level. Within the Ti electrode regime, the Fermi level is lifted up slightly toward the Dirac point since the work function of Ti (4.33 eV) is lower than that of graphene (4.5 eV). The corresponding energy difference $\Delta\phi$ between the

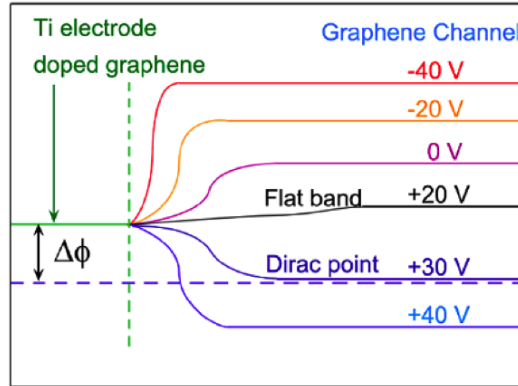


Figure 2.8 : Schematic of the surface potential

doped graphene band and the Fermi level is defined as a Schottky barrier. Since the Fermi levels of doped graphene and graphene channel are different, the band will bend in the region extending from the electrodes even for zero gate voltage. An internal electric field is formed accordingly and separates the electron-hole pairs created by incident light. As a result, a photocurrent is generated and flows into the electrodes. Its magnitude is proportional to the magnitude of the slope of the band so a maximum photocurrent always occurs at the some distance away from the source or drain which approximately corresponds to the midpoint of bending region . Meanwhile, the direction of photocurrent is determined by the sign of the slope which accounts for asymmetric lineshape since the band is bending in the opposite way at the other side. Now, if a gate voltage is taken into account, it only changes the Fermi level, or Dirac point equivalently, of graphene in the channel. For a negative gate voltage, the energy difference between graphenes near the electrode and in the channel is increased therefore the photocurrent goes up and the position of its maximum shifts close to the electrode. Similarly, it is not difficult to imagine that the photocurrent reduces and the maximal position shifts far from the electrode when a positive gate voltage is

applied. The photocurrent can be tuned to be negligible if the voltage $V_G = +20\text{V}$. In this case, the band is almost flat, as shown in Figure 2.8. Above that voltage, the bending of the band will change into the opposite direction resulting in a flip in the lineshape of photocurrent. After that, as the voltage increase further, the energy difference will be enlarged and the photocurrent will go up consequently.

2.5 Plasmonic Enhancement

The comparison of photocurrents between graphene-antenna hybrid devices and bare graphene device Figure 2.6 obvious indicates that optical antenna dramatically improves the performance of light harvesting, especially for heptamer, which can achieve up to 800% enhancement. Such significant enhancement can be attributed to two basic processes related to LSPs excitation in the optical antenna. One is the intense near-field provided by the plasmons boosts the direct excitation (DE) of electron-hole pair in the graphene. The other is hot electrons (HE) resulting from the plasmon decay transfer directly from antenna to the conduction band of graphene. The latter process is the key factor that makes the heptamer capable of providing much larger enhancement than dimer since heptamer possesses Fano resonance [13].

Fano resonance, first discovered by Ugo Fano in his study of the autoionizing states of atoms [40], exhibits a unique asymmetric shape described as [41],

$$\frac{(F\gamma + \omega - \omega_0)^2}{(\omega - \omega_0)^2 + \gamma^2} \quad (2.4)$$

where ω_0 and γ denote the position and width of the resonance, respectively; F is Fano parameter. Basically, Fano resonance is a result of the interference of a broad spectral continuum with a narrow discrete resonance. This interference can be either constructive or destructive, depending on F , which controls the degree of asymmetry

of the line shape [42]. For a plasmonic system, usually, the spectral continuum is associated with a superradiant mode which is very broad because of its large radiative damping while the discrete resonance is related to a subradiant mode whose line width is very narrow due to its lack of radiation.

In order to demystify the characteristics of Fano resonance in heptamer, we perform a numerical simulation with commercial software COMSOL Multiphysics based on finite element method (FEM). All the disks are set 130 nm in diameter and the interparticle gap is set 15 nm. The material of disks is gold whose optical constant is taken from Johnson and Christy's empirical data [43]. A linearly polarized electromagnetic plane wave is normally incident on the heptamer and the entire simulation domain is surrounded by a perfectly matched layer absorbing boundary conditions. The charge distribution is calculated with Gauss's theorem applying at the surface of the structures. The scattering spectra are obtained by integrating the intensity of scattered field after performing the near-field to far-field transformation with Stratton-Chu formula [44]. As we can see in Figure 2.9, the charge distribution shows that for the superradiant mode of heptamer, the dipole moment in each disk orients in the same direction so that the total dipole moment of heptamer is very large. It can efficiently couple to the light and thus leads to a broad spectra. On the contrary, in the subradiant mode, the dipole moments of disks at the top and bottom orient antiparallel to that of center disks thus they cancel each other. The resulting small total dipole moment couples to the light very weakly, so it can only produce a narrow peak in the spectrum. When these two modes interact with each other, they give rise to a sharp dip within a broad peak in the scattering spectra, as shown in Figure 2.9, if the interference is destructive. To some extent, a transparency window is induced around the Fano resonance, so that it can bring more light to interact directly with

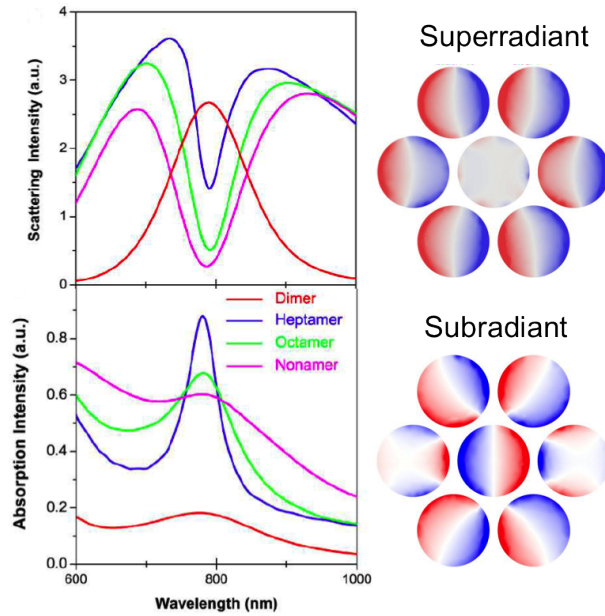


Figure 2.9 : Fano resonance in clusters

graphene. Meanwhile, the absorption of the system is enhanced at the Fano resonance since the subradiant mode loses the capability of coupling light. Consequently more hot electrons can be produced. Based on Figure 2.9, it is not difficult to imagine that an even greater enhancement can be achieved for the nonamer antenna since it has a much deeper Fano resonance.

Furthermore, another advantage of plasmonic clusters lies on their selective resonance enhancement. By properly designing the size of heptamer, photocurrent is enhanced only around intended wavelength which is available to be tuned from visible to near infrared. As demonstrated in Figure 2.10, we observed the shift of photocurrent enhancement from 650 to 950 nm linear if the size of device fabricated is varied from 80 to 180 nm in diameter. The calculated absorptions show the same tunability. Since Fano resonance of heptamer is mainly owing to the subradiant mode, the width of resonance is relatively narrow in comparison with the resonance arising

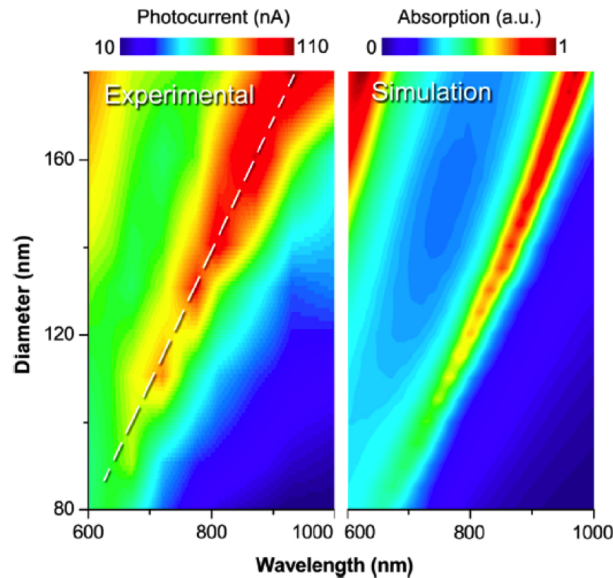


Figure 2.10 : Selective resonance detection for different sizes of heptamers

from the dimer. Therefore, to some extent, this hybrid device with heptamer antenna may provide high sensitivity in wavelength that makes it of great promise for optical detectors.

2.6 Quantum Efficiency

Now that we have qualitatively known the photocurrent enhancement results from both direct excitation and hot electrons, it will be even better to quantitatively know the exact contribution from each part. Unfortunately, the exact HE contribution cannot be calculated explicitly since our knowledge of the potential barrier at the gold graphene interface is insufficient. To circumvent this issue, the HE contribution should be inferred from the DE contribution because the total contribution is already known. Therefore, more realistic simulations are performed with commercial finite-difference time-domain (FDTD) software Lumerical FDTD Solution. The configuration, as

illustrate in Figure 2.11, consists of an optical antenna on a graphene film with silica substrate. Here, the thickness of graphene film is set as 2 nm although strictly

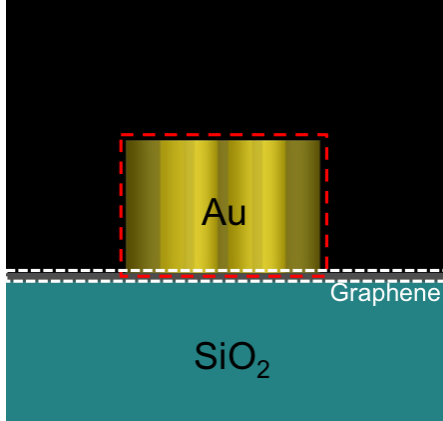


Figure 2.11 : Configuration of FDTD simulation

speaking it should be 0.5 nm. We have tested the cases for other thicknesses and find the ultimate results are consistent as long as the product of the conductivity (σ) and the thickness (d) of graphene equals the universal constant conductance. That is,

$$\sigma = \frac{\sigma_{2D}}{d} = \frac{e^2}{4\hbar d} \quad (2.5)$$

where \hbar is Planck's constant. According to Fermi's golden rule, the number of carrier by local DE is proportional to the local intensity of the electric field (E^2). So the corresponding photocurrent can be expressed in terms of an integral of local field intensity over the volume of the surrounding graphene,

$$I^{DE} = C_{DE}(\lambda) \int E^2(r) dV \quad (2.6)$$

where the coefficient $C_{DE}(\lambda)$ contains the information of matrix element and density of states. Here we assume $C_{DE}(\lambda)$ is an intrinsic property of graphene and independent of the electric field intensity. It can be straightforwardly extracted from the

experimentally measured photocurrent (10 nA) for the pristine graphene case with its field enhancement illustrated in Figure 2.12. Therefore, for the case of 180 nm

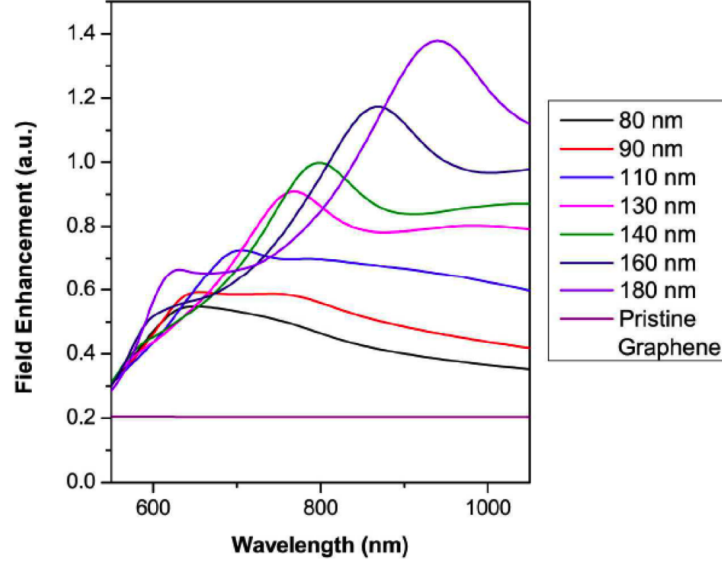


Figure 2.12 : Integral of local field intensity for graphene with and without plasmonic heptamers

disk, the photocurrent generated from DE is estimated to be 7 times larger than that of pristine graphene according to their individual field enhancement. The DE contribution to the photocurrent for different sizes of clusters are plotted with solid blue triangles in Figure 2.13 when each cluster is illuminated at its resonant wavelength.

For the HE contribution, principally, it is proportional to the optical absorption of the heptamer $S_{ABS}(\lambda)$, that is,

$$I^{HE} = C_{HE}(\lambda)S_{ABS}(\lambda) \quad (2.7)$$

where the coefficient $C_{HE}(\lambda)$ should decrease with increasing wavelength since it reflects the electron transmission across a gold-graphene interface. However, the lack of interface information along with carrier multiplication prevents it from being obtained

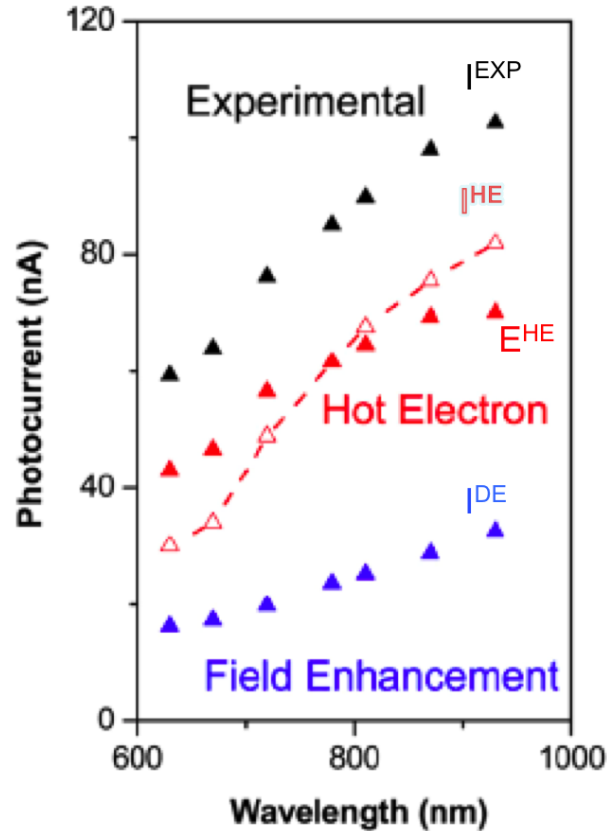


Figure 2.13 : Measured photocurrent and its different contributions

directly. Once hot electrons are excited, their distribution spans the energy interval $[\epsilon_F, \epsilon_F + \hbar\omega]$. The initial hot electron may lose some energy by exciting another hot electron just like in an Auger process [21]. As a result, one hot electron can multiply to more than one hot electrons. So the only way to get the HE contribution (solid red triangles in Figure 2.13) is $E^{HE}(\lambda) = I^{EXP}(\lambda) - I^{DE}(\lambda)$, where $I^{EXP}(\lambda)$ is the measured photocurrent. Consequently, the C_{HE} at 785nm corresponds to 113% hot electron production efficiency. Assuming this efficiency holds for all the wavelength, the value of photocurrent I^{HE} can be estimated from the absorption, as plotted in hollow red triangles in Figure 2.13. As we can see, it is well consistent with E^{HE} . By

comparing these two contributions, it is easy to notice that HE plays a more important role in photocurrent production, especially for small size heptamer. As the size of heptamer increases, the ratio between HE and DE contributions becomes lower, which is comprehensible since the absorption tends to be less predominant in a large system [45].

No matter whether DE or HE dominates the system, quantum efficiency is the figure of merit to evaluate the overall performance of the graphene-antenna device. Basically, there are external quantum efficiency (EQE) and internal quantum efficiency (IQE) [46]. For EQE, it is defined as the number of carriers produced per incident photon,

$$\eta_e = \frac{I_{exp}/q}{S_{inc}/h\nu} \quad (2.8)$$

where I_{exp} is the measured photocurrent, q is the elemental charge, S_{inc} is the incident optical power, and ν is the optical frequency. While for IQE, it is defined as the number of carriers produced per absorbed photon,

$$\eta_i = \frac{I_{exp}/q}{S_{abs}/h\nu} \quad (2.9)$$

where S_{abs} is the absorption. Since IQE relies more on its intrinsic optoelectronic properties, we implement IQE to assess the performance of our devices. The results in Figure 2.14 show the efficiency is very remarkable. It has 5-10% on average and reaches up to 22% for a device with a disk diameter of 80 nm at its resonant wavelength 630 nm.

2.7 Summaries

In this chapter, we show the optical antenna increases the quantum efficiency of light harvesting process significantly by either the plasmon-enhanced direct excitation

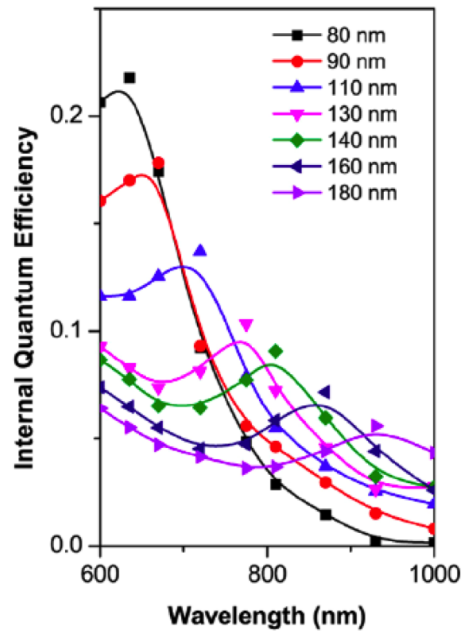


Figure 2.14 : Internal quantum efficiency

or plasmon-induced hot electron transfer. With the help of theoretical calculation and numerical simulation, we manage to separate these two factors and find the hot electrons play the predominant role. Beside we notice this hybrid-antenna device has high tunability.

Chapter 3

Optical Induced Doping with Hot Electrons

3.1 Doping and Dirac Point Shift

The most attractive feature of graphene lies in its tunable optical and electrical properties due to the tunability of its Fermi level. As we have already seen in Figure 2.8, once graphene is connected to the voltage supply, the electrons will inject into or flow out of the graphene, resulting in either electron doping or hole doping based on the sign of the gate voltage. Aside from applying a gate voltage, denoted as electrostatic doping, hot electrons generated from antennas are also able to dope the graphene although most of them preferentially flow into the electrodes without relaxation. To shed some light on this process, we pay attention to the variation of Dirac point with different conditions. The fundamental method to characterize the position of Dirac point is measuring the drain current with respect to different gate voltages at a fixed source-drain voltage 1mV, as shown in Figure 3.1. When we apply a positive gate voltage to the graphene and gradually increase it, we observe a decrease followed by an increase in the measured current. It can be explicitly understood from the energy diagram of graphene, as illustrated in the left panel of Figure 3.2. Initially, for a pristine graphene, it is p-doped due to the substrate and fabrication process. So the majority carriers are holes and its Fermi surface stays in the valence band below the Dirac point. By applying a gate voltage, electrostatic doping offers free electrons to recombine with holes in the graphene. As a result, the Fermi level increases and

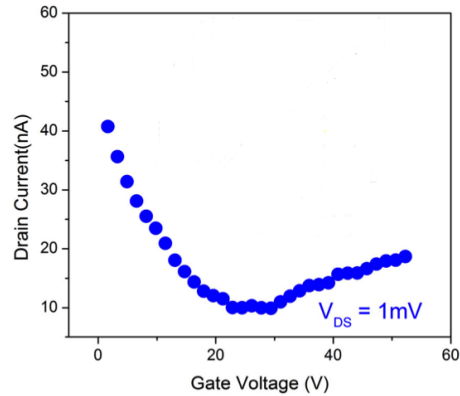


Figure 3.1 : Electrical transport characteristic $I - V_g$ curve

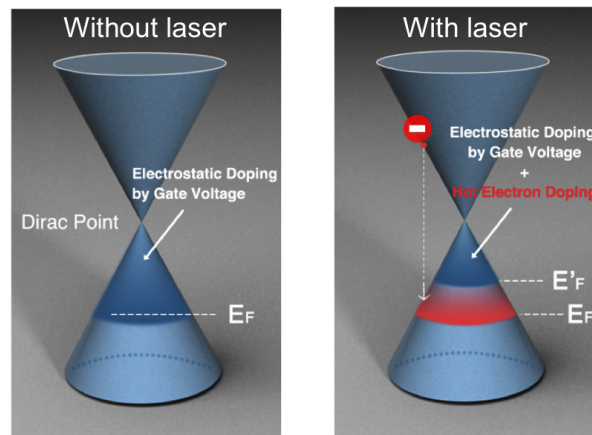


Figure 3.2 : Schematic of electrostatic doping and hot-electron doping in graphene

the carrier density decreases, leading to a drop in current. The current continuously decreases with increasing gate voltage until the Fermi surface is lifted up to the Dirac point. After that, the Fermi surface enters the conduction band and thus the majority carriers change into electrons. As gate voltage increases, the electron density increases and the current starts to rise back. At that turning point, the graphene is completely neutralized, consequently, its carrier density should approach zero except for thermal fluctuation. A minimum current occurs and the corresponding voltage

V_D is regarded as a signature of Dirac point, which is usually around 30 V.

Now, if the optical antenna is shined by a laser, hot electrons will be generated and directly transfer into the conduction band of graphene. Most of them swiftly flow out through source and drain, however a few ultimately residue in the graphene and recombine with holes, as shown in the right panel of Figure 3.2. Consequently, the original Fermi surface is lifted up by those photo-induced dopants. By performing the same measurement of drain current with respect to gate voltage, a similar minimum can be obtained, but the corresponding voltage is smaller since the initial Fermi surface is higher than that without laser. This observed voltage change is defined as Dirac point shift, which has been found in hole doping process with quantum dots [47].

The amount of Dirac point shift can be estimated semi-quantitatively. Assuming the electrostatic (ES) doping process is similar to charging a parallel-plate capacitor, the number of electrons N_{ES} doped into the graphene is proportional to the gate voltage V_g like this,

$$N_{ES} = \frac{C_g V_g}{e} \quad (3.1)$$

where $C_g = 2.4 \times 10^{-14}$ F is the capacitance between the graphene and the back gate. Without laser, the total number of electrons doped into the graphene equals to that arising from electrostatic doping. However, if the laser is on, that total number should be divided into two parts, one from electrostatic doping as before and the other from hot electron (HE) doping. Apparently, the number owing to HE (N_{HE}) should be proportional to the rate of HE generation (R_{HE}). So, the total number is written as,

$$N = \frac{C_g V_g'}{e} + \tau R_{HE} \quad (3.2)$$

where τ is a coefficient representing a time scale. Since the initial state of graphene is

the same for both cases with and without laser, the total number of electrons doped should be invariant. This implies the gate voltages V_g and V'_g in two respective cases are different. The voltage difference, corresponding to Dirac point shift, is closely related to the rate of HE production in the following way,

$$\Delta V = |V_g - V'_g| \propto R_{HE} \quad (3.3)$$

It is easy to imagine that such Dirac point shift is proportional to the absorption cross section S_{ABS} of the optical antenna due to the fact that S_{ABS} determines the R_{HE} , as we will notice in the following experimental results.

3.2 Observation of Dirac Point Shifting with Absorption

In order to demonstrate hot electron doping, gold nonamers are fabricated on the graphene to serve as optical antennas. For the nonamer, the central disk has 190 nm in diameter while eight surrounding disks have 112 nm in diameter. The separations of disks are all kept as 15 nm and all the disks have 30 nm thickness. It gives rise to a pronounced Fano resonance around 785nm, as illustrated in Figure 3.3.

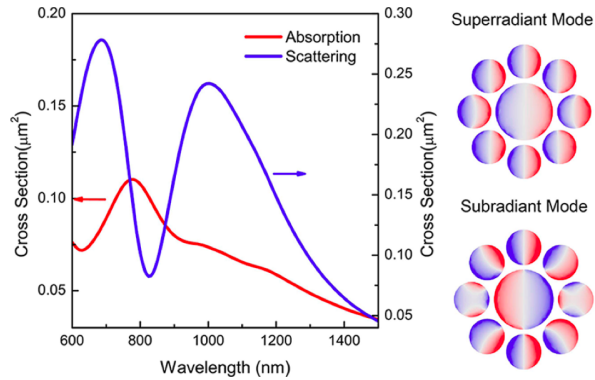


Figure 3.3 : Characteristics of Fano resonance in a plasmonic nonamer

The source-drain current with respect to gate voltage is measured under the laser illumination of wavelengths ranging from 550 nm to 1064 nm. The obtained data plotted in Figure 3.4 (a) clearly reveal the Dirac point shifts to a lower gate voltage. This behavior exactly confirms that the new carriers doped into the graphene are

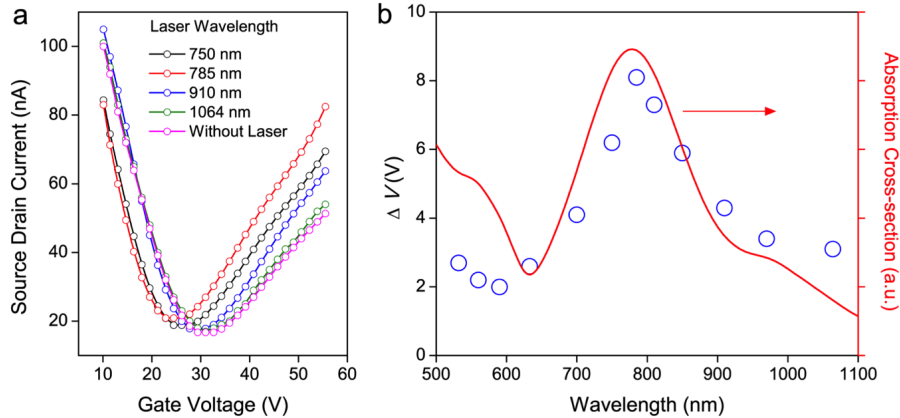


Figure 3.4 : Dirac point shift with respect to wavelength of incident laser

electrons. Besides, the amount of shift varies with wavelength and it reaches a maximum $\Delta V \approx 9V$ around 785 nm. More data related to wavelength have been extracted and plotted in Figure 3.4 (b). They are very close to the absorption cross section of the nonamer and the maximum Dirac point shift coincides with the plasmon resonance. So the physical origin of the Dirac point shift should be hot electron doping resulting from the nonradiative plasmon decay. Moreover, the hot electron doping process exhibits high tunability in terms of the antenna sizes, as shown in Figure 3.5. Here, the diameter of central disk varies from 170 to 270 nm and the diameter of the peripheral disks is changed accordingly to keep the gap size at 15 nm. The results show clearly the Dirac point shift increases with enlarging disk sizes, which is consistent with the fact that nanoantennas of larger size are capable of providing

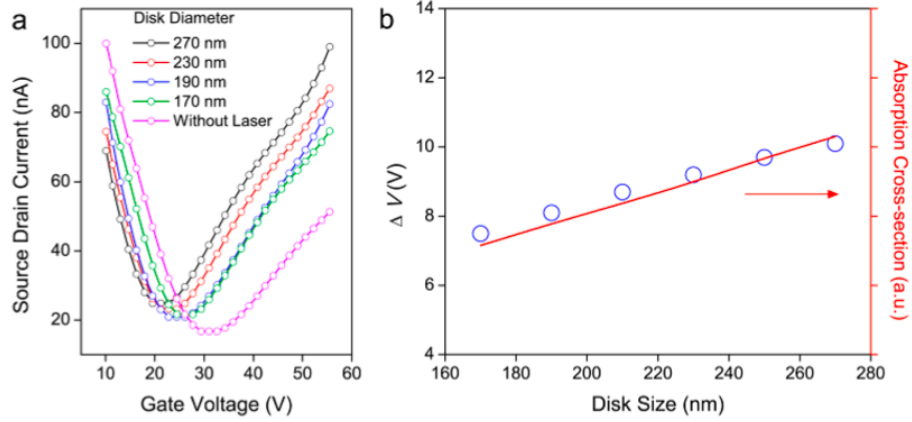


Figure 3.5 : Dirac point shift with respect to antenna size

more absorption cross-section.

3.3 Efficiency of Hot Electron Doping

Aside from the obvious Dirac point shift, more information concerning the graphene, such as the Fermi surface and the efficiency of hot electron doping, can be inferred from the data of electrical transport characteristic in Figure 3.4. Given that the Fermi surface is across the Dirac point at voltage V_D , the Fermi energy at other gate voltages can be calculated in terms of their difference from V_D by formula [35],

$$E_F = \pm \hbar v_F \sqrt{\frac{\pi C_g |V_g - V_D|}{eA}} \quad (3.4)$$

where A is the device area. Correspondingly, the carrier density associated with that gate voltage can be also expressed in terms of voltage difference as follow,

$$n = \frac{Q}{eA} = \frac{C_g |V_g - V_D|}{eA} \quad (3.5)$$

Usually, the larger the carrier density, the larger the source-drain current will be. So the difference of current from any gate voltage to the Dirac point is proportional to

the total carrier density. To get the carrier density change due to the hot electron doping, all the I-V curves with laser should be displaced vertically so that their Dirac points locate at the same height as that of the curve without laser. Then, the voltage difference between with and without laser excitation reflects the variation of the carrier density based on Eq.(3.5). The extracted carrier density change with respect to Fermi energy, determined from the I-V curve without laser, is shown in Figure 3.6. Obviously, plasmons can greatly assist doping process since a maximum of carrier

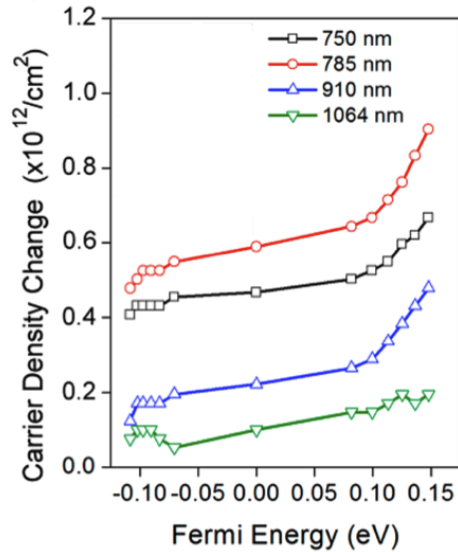


Figure 3.6 : Optical induced carrier density change with respect to Fermi energy for several wavelengths

density change achieves at resonant wavelength. Besides, it can be noticed that the carrier density changes more for n-type graphene, which shows n-type graphene has larger hot electron doping efficiency than p-type one. A possible explanation for that is the intraband relaxation where hot electrons dope the n-type graphene is much faster than interband relaxation where hot electrons dope p-type graphene [48]. The corresponding short relaxation time for intraband transition leads to a high efficiency

for the doping in n-type graphene. Moreover, the time scale τ , representing the inverse recombination rate of the hot electron-doped charge carriers, can be estimated approximately according to carrier density change. For p-type graphene $\tau \sim 2\mu\text{s}$ while for n-type graphene $\tau \sim 3\mu\text{s}$. This estimation is very coarse and the time scale characterizes the total time of three distinct processes, namely (i) hot electron generation arising from plasmon decay; (ii) hot electron transfer from the gold antenna to the graphene; and (iii) the injection of hot electron into the band of graphene. However, compared to reports on hole doping process (10 ms) induced by quantum dots [36,47], hot electron doping is comparably faster and expected to be a promising candidate for fast optoelectronic devices.

3.4 Saturation of Hot Electron Doping

The Dirac point shift also depends on the power of incident laser since the absorption of optical antenna is proportional to it. By tuning the power of 785 nm laser from 0 to 50 μW , the Dirac point shifts are recorded in Figure 3.7. As we can see, the

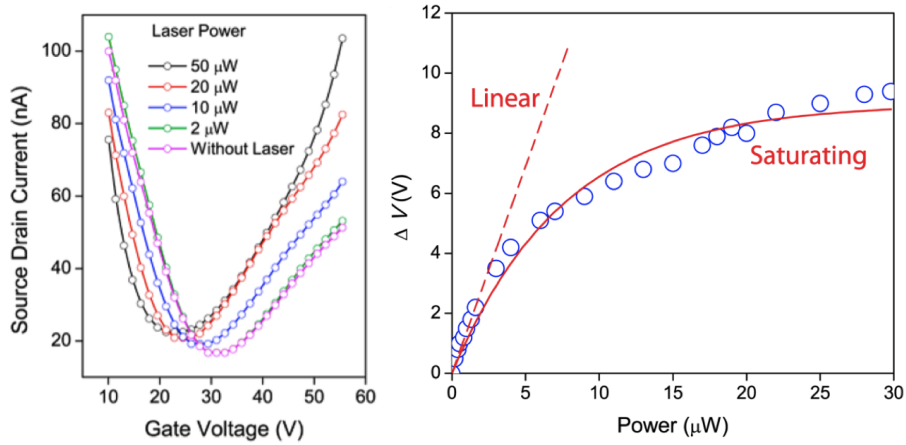


Figure 3.7 : Dirac point shift varies with incident laser power

Dirac point shift changes linearly with the power at first until $5 \mu\text{W}$. Above that, this linear relationship no longer holds and an apparent nonlinear characteristic appears. For even higher incident power, the Dirac point shift tends to saturate. Two possible explanations may account for this. First one is regarding to the recombination process, as shown in the left panel of Figure 3.8. As the power goes up, more hot

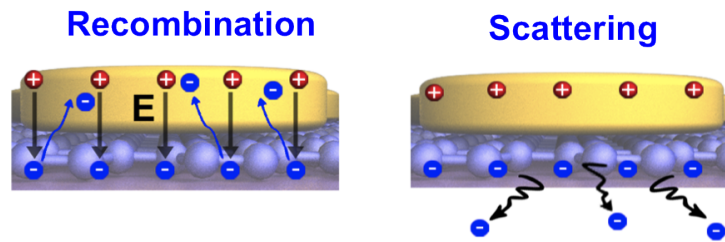


Figure 3.8 : Schematics of recombination and scattering processes

electrons are generated and thus dope into the graphene. The large number of hot electron dopants in graphene causes negative charge accumulation there while leaves many holes in the gold to form positive charges. These positive and negative charges build up an internal electrostatic field that prohibits the hot electrons from further transferring into and doping the graphene. The other explanation is related to the electron-electron scattering as depicted in the right panel of Figure 3.8. Since there are excessive electrons residing in the graphene, they will repulse the new injected hot electron according to the Coloumbic interaction. As a result, the scattering between electrons prevents hot electrons doping the graphene. Eventually, both processes make doping process exhibit saturation properties.

3.5 Optically Induced Electronics

By patterning graphene with metallic antenna and quantum dots, two different hot carriers, electrons and holes, can be injected into the graphene respectively to form n-type and p-type materials. Since p-type and n-type semiconductors are two building blocks for electronics, simple electronic elements can be constructed by incorporating these two types of hybrid materials. More importantly, these electronic elements are capable of optical controlling, as illustrated in Figure 3.9. As we can see for the

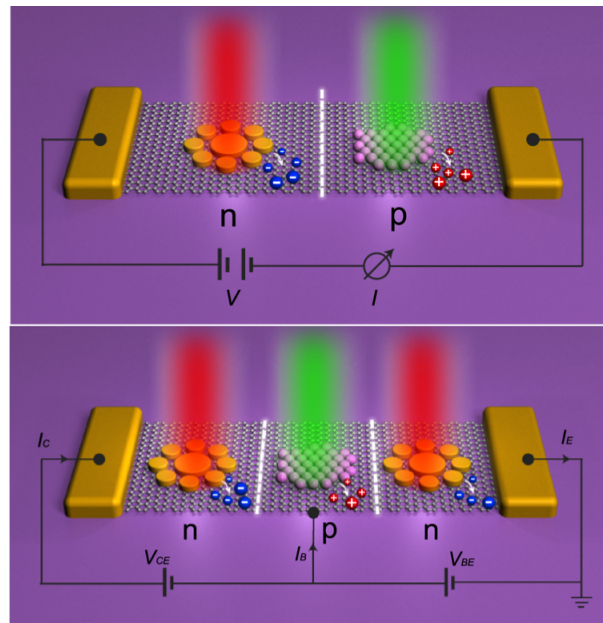


Figure 3.9 : Optical induced diode and transistor

diode, the graphene is just like homogenous semiconductor without light excitation and the current can pass through it from any direction. But, if the light of specific wavelength is shined on it, graphene sheet changes into inhomogenous material with a p-n junction in the middle. Accordingly, current is allowed in only one direction while forbidden in another. So the device is actually switched on and off by light. It

is the same for a transistor.

3.6 Summaries

In this chapter, we have demonstrated hot electrons generated from optical antenna can dope the electronic band of the graphene. The efficiency of doping process is controlled by various parameters such as size and resonant frequency of the antenna, power of the light, and Fermi energy of graphene as so on. Moreover, the short doping time makes this hybrid structure very competitive in optoelectronic application especially when it is combined with hole doping materials to build complex optical circuitry.

Chapter 4

Conclusion

In the thesis, we investigated the optoelectronic properties of a hybrid device consisting of pristine graphene sheet and optical antenna. We found the plasmons excited in optical antenna could significantly affected the properties of graphene, especially by means of hot electrons arising from plasmon decay. The metallic oligomers we used as optical antenna, on the one hand, exhibited great tunability across the near-infrared to the visible regime. On the other hand, they provided fascinating Fano resonance which not only enhanced optical near-field but also gave large hot electron production by a increase in optical absorption.

In comparison with antennaless graphene device, we observed optical antenna could give rise to an 800% enhancement of the photocurrent generation, corresponding to internal quantum efficiency ranging from 5 to 20%. The numerical simulations with FEM and FDTD method enable us to attribute the improvement of light-harvesting efficiency to plasmon-enhanced direct carrier excitation in graphene as well as plasmon-induced hot electron transfer from optical antenna. Furthermore, we calculated individual enhancement for each part and found the hot electron process accounted for two thirds of the total enhancement, dominating the overall photocurrent generation.

Meanwhile, we also showed the plasmon-induced hot electron transfer could dope the graphene so as to make its electronic property change. Measurement of its electrical transport characteristic revealed the plasmon-induced doping could shift the Dirac

point as much as 10V corresponding to electrostatic doping. Besides, this Dirac point shift bore nonlinear characteristic with respect to the power of incident laser. And we found the n-type graphene had a larger doping efficiency than p-type one. Moreover, the doping time of hot electrons was estimated to be about microsecond which is much faster than hole doping with quantum dots.

Since the hybrid graphene-antenna device possesses good tunability, its optical performance could be even better after further optimization. It may be implemented as active tuning and switching optoelectronic devices in future.

Bibliography

- [1] A. Polman, “Plasmonics applied,” *Science*, vol. 322, no. 5903, pp. 868–869, 2008.
- [2] S. A. Maier, *Plasmonics: fundamentals and applications*. Springer, 2007.
- [3] W. L. Barnes, A. Dereux, T. W. Ebbesen, *et al.*, “Surface plasmon subwavelength optics,” *Nature*, vol. 424, no. 6950, pp. 824–830, 2003.
- [4] D. K. Gramotnev and S. I. Bozhevolnyi, “Plasmonics beyond the diffraction limit,” *Nature Photonics*, vol. 4, no. 2, pp. 83–91, 2010.
- [5] S. Nie and S. R. Emory, “Probing single molecules and single nanoparticles by surface-enhanced raman scattering,” *science*, vol. 275, no. 5303, pp. 1102–1106, 1997.
- [6] S. Pillai, K. Catchpole, T. Trupke, G. Zhang, J. Zhao, and M. Green, “Enhanced emission from si-based light-emitting diodes using surface plasmons,” *Applied physics letters*, vol. 88, no. 16, pp. 161102–161102, 2006.
- [7] M. Moskovits, “Surface-enhanced spectroscopy,” *Reviews of Modern Physics*, vol. 57, no. 3, p. 783, 1985.
- [8] H. A. Atwater and A. Polman, “Plasmonics for improved photovoltaic devices,” *Nature materials*, vol. 9, no. 3, pp. 205–213, 2010.
- [9] K. Catchpole and A. Polman, “Plasmonic solar cells,” *Optics express*, vol. 16, no. 26, pp. 21793–21800, 2008.

- [10] S. Lal, S. E. Clare, and N. J. Halas, “Nanoshell-enabled photothermal cancer therapy: impending clinical impact,” *Accounts of Chemical Research*, vol. 41, no. 12, pp. 1842–1851, 2008.
- [11] R. Bardhan, S. Lal, A. Joshi, and N. J. Halas, “Theranostic nanoshells: from probe design to imaging and treatment of cancer,” *Accounts of chemical research*, vol. 44, no. 10, pp. 936–946, 2011.
- [12] E. Prodan, C. Radloff, N. Halas, and P. Nordlander, “A hybridization model for the plasmon response of complex nanostructures,” *Science*, vol. 302, no. 5644, pp. 419–422, 2003.
- [13] J. A. Fan, C. Wu, K. Bao, J. Bao, R. Bardhan, N. J. Halas, V. N. Manoharan, P. Nordlander, G. Shvets, and F. Capasso, “Self-assembled plasmonic nanoparticle clusters,” *science*, vol. 328, no. 5982, pp. 1135–1138, 2010.
- [14] S. Lal, S. Link, and N. J. Halas, “Nano-optics from sensing to waveguiding,” *Nature photonics*, vol. 1, no. 11, pp. 641–648, 2007.
- [15] A. G. Brolo, “Plasmonics for future biosensors,” *Nature Photonics*, vol. 6, no. 11, pp. 709–713, 2012.
- [16] W. A. Murray and W. L. Barnes, “Plasmonic materials,” *Advanced Materials*, vol. 19, no. 22, pp. 3771–3782, 2007.
- [17] H. J. Lezec, J. A. Dionne, and H. A. Atwater, “Negative refraction at visible frequencies,” *Science*, vol. 316, no. 5823, pp. 430–432, 2007.
- [18] M. Hentschel, M. Schäferling, T. Weiss, H.-G. Kuball, N. Liu, and H. W. Giessen, “Three-dimensional chiral plasmonic oligomers,” in *Quantum Electronics and*

Laser Science Conference, Optical Society of America, 2012.

- [19] M. I. Stockman, “Nanoplasmonics: The physics behind the applications,” *Physics Today*, vol. 64, p. 39, 2011.
- [20] M. L. Brongersma and V. M. Shalaev, “Applied physics the case for plasmonics,” 2010.
- [21] C. Frischkorn and M. Wolf, “Femtochemistry at metal surfaces nonadiabatic reaction dynamics,” *Chemical Reviews-Columbus*, vol. 106, no. 10, pp. 4207–4233, 2006.
- [22] M. W. Knight, H. Sobhani, P. Nordlander, and N. J. Halas, “Photodetection with active optical antennas,” *Science*, vol. 332, no. 6030, pp. 702–704, 2011.
- [23] S. Mukherjee, F. Libisch, N. Large, O. Neumann, L. V. Brown, J. Cheng, B. Lassiter, E. A. Carter, P. Nordlander, and N. J. Halas, “Hot electrons do the impossible: Plasmon-induced dissociation of h₂ on au,” *Nano letters*.
- [24] J. Yan, M. Kim, J. Elle, A. Sushkov, G. Jenkins, H. Milchberg, M. Fuhrer, and H. Drew, “Dual-gated bilayer graphene hot-electron bolometer,” *Nature Nanotechnology*, vol. 7, no. 7, pp. 472–478, 2012.
- [25] A. C. Neto, F. Guinea, N. Peres, K. Novoselov, and A. Geim, “The electronic properties of graphene,” *Reviews of modern physics*, vol. 81, no. 1, p. 109, 2009.
- [26] K. Novoselov, A. Geim, S. Morozov, D. Jiang, Y. Zhang, S. Dubonos, I. Grigorieva, and A. Firsov, “Electric field effect in atomically thin carbon films,” *Science*, vol. 306, no. 5696, pp. 666–669, 2004.

- [27] F. Bonaccorso, Z. Sun, T. Hasan, and A. Ferrari, “Graphene photonics and optoelectronics,” *Nature Photonics*, vol. 4, no. 9, pp. 611–622, 2010.
- [28] F. H. Koppens, D. E. Chang, and F. J. Garca de Abajo, “Graphene plasmonics: a platform for strong light–matter interactions,” *Nano letters*, vol. 11, no. 8, pp. 3370–3377, 2011.
- [29] C.-F. Chen, C.-H. Park, B. W. Boudouris, J. Horng, B. Geng, C. Girit, A. Zettl, M. F. Crommie, R. A. Segalman, S. G. Louie, *et al.*, “Controlling inelastic light scattering quantum pathways in graphene,” *Nature*, vol. 471, no. 7340, pp. 617–620, 2011.
- [30] T. Echtermeyer, L. Britnell, P. Jasnós, A. Lombardo, R. Gorbachev, A. Grigorenko, A. Geim, A. Ferrari, and K. Novoselov, “Strong plasmonic enhancement of photovoltage in graphene,” *Nature Communications*, vol. 2, p. 458, 2011.
- [31] Y. Liu, R. Cheng, L. Liao, H. Zhou, J. Bai, G. Liu, L. Liu, Y. Huang, and X. Duan, “Plasmon resonance enhanced multicolour photodetection by graphene,” *Nature Communications*, vol. 2, p. 579, 2011.
- [32] Z. Fang, Z. Liu, Y. Wang, P. M. Ajayan, P. Nordlander, and N. J. Halas, “Graphene-antenna sandwich photodetector,” *Nano letters*, vol. 12, no. 7, pp. 3808–3813, 2012.
- [33] Z. Fang, Y. Wang, Z. Liu, A. Schlather, P. M. Ajayan, F. H. Koppens, P. Nordlander, and N. J. Halas, “Plasmon-induced doping of graphene,” *ACS nano*, 2012.
- [34] A. Grigorenko, M. Polini, and K. Novoselov, “Graphene plasmonics,” *Nature Photonics*, vol. 6, no. 11, pp. 749–758, 2012.

- [35] Z. Li, E. Henriksen, Z. Jiang, Z. Hao, M. Martin, P. Kim, H. Stormer, and D. N. Basov, “Dirac charge dynamics in graphene by infrared spectroscopy,” *Nature Physics*, vol. 4, no. 7, pp. 532–535, 2008.
- [36] F. Wang, Y. Zhang, C. Tian, C. Girit, A. Zettl, M. Crommie, and Y. R. Shen, “Gate-variable optical transitions in graphene,” *Science*, vol. 320, no. 5873, pp. 206–209, 2008.
- [37] N. Ashcroft and N. Mermin, *Solid state physics*. Holt-Saunders International Editions: Science : Physics, Holt, Rinehart and Winston; Saunders, 1976.
- [38] E. Prodan and P. Nordlander, “Plasmon hybridization in spherical nanoparticles,” *The Journal of chemical physics*, vol. 120, p. 5444, 2004.
- [39] F. Schwierz, “Graphene transistors,” *Nature nanotechnology*, vol. 5, no. 7, pp. 487–496, 2010.
- [40] U. Fano, “Effects of configuration interaction on intensities and phase shifts,” *Phys. Rev.*, vol. 124, pp. 1866–1878, Dec 1961.
- [41] B. Luk’yanchuk, N. I. Zheludev, S. A. Maier, N. J. Halas, P. Nordlander, H. Giessen, and C. T. Chong, “The fano resonance in plasmonic nanostructures and metamaterials,” *Nature materials*, vol. 9, no. 9, pp. 707–715, 2010.
- [42] A. E. Miroshnichenko, S. Flach, and Y. S. Kivshar, “Fano resonances in nanoscale structures,” *Reviews of Modern Physics*, vol. 82, no. 3, p. 2257, 2010.
- [43] P. B. Johnson and R. W. Christy, “Optical constants of the noble metals,” *Phys. Rev. B*, vol. 6, pp. 4370–4379, Dec 1972.
- [44] J. Jackson, *Classical Electrodynamics*. Wiley, 1998.

- [45] H. C. van de Hulst, *Light scattering by small particles*. Dover publications, 1981.
- [46] C. Scales and P. Berini, “Thin-film schottky barrier photodetector models,” *Quantum Electronics, IEEE Journal of*, vol. 46, no. 5, pp. 633–643, 2010.
- [47] G. Konstantatos, M. Badioli, L. Gaudreau, J. Osmond, M. Bernechea, F. P. G. de Arquer, F. Gatti, and F. H. Koppens, “Hybrid graphene-quantum dot phototransistors with ultrahigh gain,” *Nature Nanotechnology*, vol. 7, no. 6, pp. 363–368, 2012.
- [48] J. I. Pankove, *Optical processes in semiconductors*. Courier Dover Publications, 1971.